Dome growth, collapse, and valley fill at Soufrière Hills Volcano, Montserrat, from 1995 to 2013: Contributions from satellite radar measurements of topographic change

Article

Accepted Version

Dome growth, collapse and valley fill at Soufrière Hills Volcano, Montserrat from 1995 to 2013: contributions from satellite radar measurements of topographic change.

D.W.D. Arnold[1], J. Biggs[1], G. Wadge[2], S.K. Ebmeier[1], H.M. Odbert[3] and M.P. Poland[3]

[1]*COMET, School of Earth Sciences, University of Bristol, UK*

[2]*COMET, Department of Meteorology, University of Reading, UK*

[3]*School of Earth Sciences, University of Bristol, UK*

[4]*USGS, Cascade Volcano Observatory, Vancouver, Washington, USA*

ABSTRACT

Frequent high-resolution measurements of topography at active volcanoes can provide important information for assessing the distribution and rate of emplacement of volcanic deposits and their influence on hazard. At dome-building volcanoes, monitoring techniques such as LiDAR and photogrammetry often provide a limited view of the area affected by the eruption. Here, we show the ability of satellite radar observations to image the lava dome and pyroclastic density current deposits that resulted from 15 years of eruptive activity at Soufrière Hills Volcano (SHV), Montserrat from 1995 to 2010. We present the first geodetic observations of the complete subaerial deposition field on Montserrat, including the lava dome. Synthetic aperture radar observations from the ALOS satellite and TanDEM-X mission are used to map the

distribution and magnitude of elevation changes. We estimate a net dense-rock equivalent volume increase of 108 ± 15M m^3 of the lava dome and 300 ± 220M m^3 of talus and subaerial pyroclastic density current deposits. We also show variations in deposit distribution during different phases of the eruption, with greatest on-land deposition to the south and west, from 1995 to 2005 and the thickest deposits to the west and north after 2005. We conclude by assessing the potential of using radar-derived topographic measurements as a tool for monitoring and hazard assessment during eruptions at dome building volcanoes.

1. INTRODUCTION

At active volcanoes the rate of lava effusion acts as both an indicator of the state of the subsurface magma system and influence on the style and distribution of erupted material. At basaltic systems, effusion rate is one of the main controls of lava flow extent (e.g. Walker, 1973; Harris et al., 2007), while at andesitic domes, it controls the extrusion style and the effusive-explosive transition (Gregg and Fink, 1996; Fink and Griffiths, 1998; Watts et al., 2002; Hutchison et al., 2013). In steady-state, lava effusion rate can constrain the volume and pressure change of shallow magma reservoirs (e.g. Dvorak and Dzurisin, 1993; Harris et al., 2003, 2007; Anderson and Segall, 2011), while long-lived volcanic eruptions are often characterised by temporal variations in effusion rate or pauses in lava extrusion, which may be related to changes in the volcanic plumbing system or deeper magma supply (e.g. Sparks et al., 1998; Watts et al., 2002; Harris et al., 2003; Ebmeier et al., 2012; Wadge et al., 2014a; Poland, 2014).

Lava effusion rate is one of the more difficult eruption parameters to measure, even at well-monitored volcanoes (e.g. Wright et al., 2001; Poland 2014). Field measurements require specific conditions, such as molten lava flowing in a confined channel or lava, and provide

45 instantaneous local lava flux measurements that may not reflect the longer-term effusion rate
46 (e.g. Lipman and Banks, 1987; Kauahikaua et al., 1998; Wright et al., 2001), while satellite
47 measurements of heat flux can be used to estimate a time-averaged effusion rate (see Harris et
48 al., 2007 for a review). However, this technique needs cloud-free satellite imagery, which may
49 not be available and requires lava extent to be limited by cooling rather than topography (e.g.
50 Harris et al., 2007; Ebmeier et al., 2012).

51 Topography is a major influence on hazard from eruptive products at active volcanoes
52 (e.g. Guest and Murray, 1979; Blong, 1984; Cashman and Sparks, 2013), because local slope is a
53 primary control for gravitationally driven flows, such as lava flows, pyroclastic density currents
54 (PDCs), and lahars, influencing flow direction and velocity (e.g. Walker, 1973; Druitt, 1998;
55 Carrivick et al., 2008). At active lava domes, rockfalls and PDCs are generated primarily in the
56 direction of dome growth (Watts et al., 2002), and more generally, where the addition of new
57 volcanic material causes a topographic slope to become over-steepened, this can lead to an
58 increased risk of landslide, rockfall and sector collapse (e.g. Montgomery, 2001). The infilling of
59 valleys with volcanic deposits increases the probability of secondary lahar generation during
60 heavy rainfall (e.g. van Westen and Daag, 2005; Guzzetti et al., 2007).

61 The availability of up-to-date, high-resolution maps of the topography is therefore
62 important both for hazard mitigation as well as improving volcano mass budgets and scientific
63 understanding of volcanic processes. Knowledge of the direction volcanic flows are likely to
64 travel, and the ability to model their likely extent are greatly improved at volcanoes where a
65 high-resolution digital elevation model (DEM) is available (e.g. Stevens et al., 2003; Hubbard et
66 al., 2007; Huggel et al., 2008), and comparing changes in topography over time can provide an
67 estimate of the volume of erupted products, which may be used to estimate a time averaged

68 effusion rate (e.g. Lu et al., 2003; Harris et al., 2007; Ebmeier et al., 2012; Poland, 2014; Xu and
69 Jónsson, 2014; Kubanek et al., 2015a, 2015b; Albino et al., 2015).

70 We chose Soufrière Hills Volcano (SHV), Montserrat, to investigate changes in
71 topography due to a long-lived dome-building eruption. We use satellite radar observations to
72 constrain topographic changes due to the eruption, which allows us to track the location and
73 thickness of deposits across the whole island during the 1995–2010 eruption. Recent work has
74 shown the benefit of satellite based radar observations at volcanoes, both for monitoring
75 purposes and for improving the understanding of surface and subsurface processes (e.g.
76 Dietterich et al., 2012, Sparks et al., 2012, Biggs et al., 2014, Salzer et al., 2014, Pinel et al.,
77 2015). The 1995–2010 eruption of SHV has been particularly well studied using a wide variety
78 of techniques, which enables us to assess the relative advantages and disadvantages of using
79 satellite geodesy specifically for topographic measurements at active volcanoes.
80

81 **2. BACKGROUND**

82 Soufrière Hills Volcano (SHV), Montserrat, is a Peléean lava dome complex that has
83 been erupting intermittently since 18 Jul. 1995. At the time of writing, despite the lack of lava
84 extrusion since 11 Feb. 2010, it is not clear that the eruption sequence has ended due to high SO_2
85 flux (Wadge et al., 2014a). The eruption so far has been characterised by five extrusive phases
86 lasting up to three years separated by months to years of quiescence (Fig. 1c) (Wadge et al.,
87 2014a). Activity is characterised by lava dome growth and collapse, with Vulcanian explosions
88 and PDCs (Sparks et al., 2002). Wadge et al., (2014a) and references therein provide a more
89 detailed description of recent activity at SHV.

90 The topography has changed markedly over 15 years of lava extrusion. The height of the
91 lava dome has varied by over 400 m (Wadge et al., 2014a)(Fig. 1c), and some valleys radiating
92 outward from the volcano have been infilled by over 100 m of new material (Wadge et al., 2010,
93 2011). Previous large dome collapse events at SHV (> 10M m^3) have only occurred when the
94 summit of the lava dome is greater than 950 m above sea level (asl) (Wadge et al., 2010). The
95 summit of the current lava dome has been 1083 m asl since the end of Phase 5 in Feb 2010
96 (Stinton et al., 2014); therefore, there remains a possibility of large collapse should lava
97 extrusion resume. This may pose a risk to human life if PDCs generated by the collapse are
98 directed northwest towards inhabited zones at the bottom of the Belham River Valley (Fig. 1).
99 Approximately 1 km^3 of magma was emitted during 1995–2010, dispersed in a variety of
100 deposits (Wadge et al., 2014a; Odbert et al., 2015). Knowledge of the past and present
101 distribution and redistribution of this volume is important at SHV, where the evolution of the
102 topography and modification of drainages during the eruption has had a key impact on the hazard
103 from PDCs and surges, lahars, and dome collapses (e.g. Cole et al., 1998; Wadge et al., 2011;
104 Ogburn et al., 2014). Loading from volcanic deposits on Montserrat also has an effect on the
105 long-term deformation trend observed by GPS (Odbert et al., 2015). It is important to understand
106 the distribution of these deposits over the course of the eruption so that appropriate corrections
107 can be made to the GPS time series.
108
109 **3. PREVIOUS TOPOGRAPHIC MEASUREMENTS ON MONTSERRAT**
110 The topography of Montserrat has been represented and recorded in several digital
111 elevation models (DEMs) acquired using a combination of ground based and airborne sensors
112 (Table 1) and also satellite platforms (Table 2). The eruption spans most of the duration of the

satellite InSAR era, which began in 1992, and so provides a good example of the capabilities and limitations of using various sensors to measure topography and deposit volumes at an active volcano. Previously published ground and air-based DEMs are used as a reference level for the generation of new satellite-derived DEMs, discussed in section 4.

3.1. Ground- and air-based

Long-term operational measurements of the lava dome shape and height have been made using both ground-based and helicopter-based photogrammetry (e.g. Sparks et al., 1998; Ryan et al., 2010; Stinton et al., 2014). Comparing the difference between photographs taken from a continuously recording camera in the same position at different times revealed changes to the dome morphology (Wadge et al., 2009). Using theodolite measurements of the dome in combination with photogrammetry reveals profile changes of the dome height (Fig 1c) and can constrain estimates of changes in the dome volume. However, because the technique is optical, line of sight to the dome is needed; therefore, no observations can be made at night or if the dome is obscured by meteoric clouds or volcanic emissions (e.g. Ryan et al., 2010; Wadge et al., 2014b).

Operational photogrammetry observations of SHV have been episodically supplemented with light detection and ranging (LiDAR) measurements. LiDAR uses a laser scanner to detect the distance to a network of points, which can then be converted into a DEM. The laser scanner can either be ground-based (Jones, 2006) or airborne (Odbert and Grebby, 2014). LiDAR can achieve data densities up to ten times greater than photogrammetry (Jones, 2006); however, LiDAR also requires optical line of sight to the ground surface and gaps in the data due to obstruction of the volcano can be problematic. Cloud cover is also an issue in airborne surveys;

for example, in the 2010 airborne LiDAR survey of Montserrat, the helicopter was unable to fly above the cloud base, preventing data retrieval above 700 m asl and resulting in a gap in the DEM over the lava dome (Cole et al., 2010).

One method of measuring topography, even through clouds or at night, is to use an active radar signal. AVTIS (All-weather Volcano Topography Imaging Sensor) is a millimetre-wave ground-based radar sensor specifically designed to measure the topography and temperature of the lava dome on Montserrat (Wadge et al., 2005). AVTIS measurements of topography were used to generate DEMs of the lava dome in 2005, 2006, and 2008 and to monitor the eruption during Phase 3 (Wadge et al., 2008). Repeated measurements of topography were used to estimate an apparent average lava extrusion rate of 3.9 m^3s^{-1} between November 2005 and April 2006. Due to instrument rebuilding and shipping delays, there were no AVTIS measurements of the dome during Phases 4 and 5 (Wadge et al., 2014b). Post-Phase 5 measurements of topography from a fixed AVTIS installation have been used to image and quantify mass wasting of the lava dome (Wadge et al., 2014b).

DEM difference maps have been used to map deposits on Montserrat and to estimate deposit thicknesses between the start of the eruption and Feb. 1999 (Wadge et al., 2002) and between 1995 and 2010 (Odbert et al., 2015). The usefulness of this approach is limited due to sparse sampling of DEMs in time (and sometimes space), predominantly because of the logistics of ground-based methods, and the expense of air-based methods.

3.2. InSAR

Interferometric synthetic aperture radar (InSAR) is a technique that measures the change in radar phase caused by differences in path length between two radar scenes acquired with

159 similar viewing geometries. The geometric contribution to phase in the resulting interferogram
160 can be used to estimate the topography of the ground surface and to create DEMs. In order to
161 determine topography using InSAR, the backscattering properties of the surface must be stable
162 over time (coherent). Where the ground surface varies over time (e.g., through vegetation growth
163 or slope change), the phase return from each pixel between different images will be effectively
164 random, and no meaningful signal can be retrieved (e.g. Wang et al., 2010).

165 In rugged volcanic settings, loss of signal can be caused by suboptimal viewing
166 geometry. Where slopes facing the sensor are steeper than the radar incidence angle, reflections
167 from the top of the slope will be received before reflections from the base, resulting in loss of
168 signal known as layover. Conversely, slopes facing away from the satellite at an angle steeper
169 than the incidence angle will instead have shadow zones, where no signal is reflected and
170 therefore no data are retrieved (e.g. Bürgmann et al., 2000; Ebmeier et al., 2013a; Pinel et al.,
171 2014).

172 Since the early 1990s there have been several satellite-based InSAR platforms, many of
173 which have acquired data over Montserrat (Table 2). Previous C-band (wavelength 5.6 cm)
174 InSAR studies of Montserrat have been hampered by poor coherence due to dense vegetation and
175 rapid topographic change around the active lava dome, and they have therefore only been able to
176 recover topography on surfaces covered by post-1995 volcanic deposits, and for periods
177 spanning less than 100 days (Wadge et al., 2002, 2006a). L-band (wavelength 23.6 cm) data
178 from the PALSAR (Phased Array type L-band Synthetic Aperture Radar) instrument on the
179 JAXA (Japan Aerospace eXploration Agency) satellite ALOS provide better coherence in
180 densely vegetated tropical settings (e.g. Parks et al., 2011; Ebmeier et al., 2013b, Chaussard et
181 al., 2013). Fournier et al., 2010, performed a preliminary survey of the Lesser Antilles arc using

ALOS data and observed that temporal decorrelation of signal was still a significant problem, with interferograms spanning a period longer than one year becoming almost completely incoherent due to rapid vegetation growth.

One method to mitigate against temporal decorrelation is to use two sensors separated in space rather than time. The Shuttle Radar Topography Mission (SRTM) used two antennae separated by 60 m to create the first global DEM, with a grid spacing of 90/30 m (Farr et al., 2007). A recent higher-resolution alternative is provided by the DLR (Deutsches Zentrum für Luft- und Raumfahrt e. V.; German Space Agency) satellite pair TerraSAR-X (TSX) and TanDEM-X (TDX), following the launch of TDX on June 21, 2010. The two satellites orbit the Earth in close formation and operate in bistatic imaging mode, where one satellite transmits a radar signal and both satellites simultaneously receive the reflected signal. The maximum horizontal resolution is 2–2.5 m (Krieger et al., 2007). Interferograms formed from bistatic image pairs have no loss of signal due to temporal decorrelation, which makes TanDEM-X a good tool for measuring topography on Montserrat.

4. METHOD

4.1. Measuring topographic change with InSAR

An interferogram contains phase contributions from differences in viewing geometry between two different satellite positions. The contributions to the measured phase change $\delta\phi$ at each pixel in an interferogram are given by equation 1 (e.g. Massonnet and Feigl, 1998; Bürgmann et al., 2000):

$$\delta\phi = \delta\phi_{def}+\delta\phi_{orbit}+\delta\phi_{atm}+\delta\phi_{pixel}+\delta\phi_{topo}. \quad (1)$$

where $\delta\phi_{def}$ is a deformation phase contribution caused by displacement of the ground surface between the time of image acquisitions; $\delta\phi_{orbit}$ is an orbit contribution due to the curvature of the Earth's surface (easily removed with a 'flat earth' correction during processing); $\delta\phi_{atm}$ is an atmospheric component mainly caused by changes in tropospheric water vapour between scenes; $\delta\phi_{pixel}$ is a pixel-dependent contribution due to changes to the scattering properties of the ground surface within that pixel; and $\delta\phi_{topo}$ is a topographic component due to the effect of viewing topography from a different angle in different acquisitions — an effect that can be estimated using a DEM and then removed.

If $\delta\phi_{topo}$ is incorrectly estimated from a DEM, then even after that component is subtracted there will be a residual topographic contribution, or 'DEM error,' within an interferogram. Where there has been significant topographic change between the DEM and InSAR acquisitions, the DEM error will represent a real change in elevation of the ground surface (e.g. Ebmeier et al., 2012). At an active volcano such as SHV, this change will either be positive, caused by topographic growth due to the emplacement of new material through lava dome extrusion and infilling of valleys by volcanic deposits, or negative due to removal of material through erosion and gravitational collapse events. Radar phase is only coherent for stable, solid reflectors; therefore, no data are recovered for submarine deposits.

Unlike phase contributions from ground deformation or atmospheric noise, these DEM errors will be linearly correlated with the perpendicular baseline between the two radar paths (B_{perp}). The gradient of this correlation is a combination of the range from the satellite to the ground (r), the radar wavelength (λ), the incidence angle (v), and the vertical difference in elevation (δz) between the DEM used for InSAR processing and the residual topographic signal (e.g. Bürgmann et al., 2000)(Equation 2).

$$\delta\phi_{topo} = \frac{k\, B_{perp}}{r\lambda \sin v}\delta z. \quad (2)$$

The factor k is a constant relating to the radar path length. For the repeat-pass monostatic case (e.g., ALOS), k is 4π, whereas for the single-pass bistatic case (e.g., TanDEM-X), both satellites share a common radar path so k is 2π (e.g. Hanssen, 2001; Kubanek et al., 2015a).

Crustal deformation rates on Montserrat are low (< 2 cm/year measured by GPS) during periods of quiescence (Odbert et al., 2014). If we assume that the phase contributions from deformation and atmospheric noise are small compared with the topographic contribution, we can rearrange equation 2 to convert the phase contribution $\delta\phi_{topo}$ into the vertical topographic change, δz.

For a set of n interferograms, equation 2 can be written in the form $\mathbf{d} = \mathbf{Gz}$, where $\mathbf{d}$ is a $n\times1$ column vector containing the phase change in each interferogram, $\delta\phi$, and $\mathbf{G}$ is a $n\times1$ design matrix, that contains the corresponding perpendicular baselines, B_{perp}, and a constant of proportionality given by $r\lambda\sin v / 4\pi$, and $\mathbf{z}$ is the vertical height change.

We solve $\mathbf{d}=\mathbf{Gz}$ for $\mathbf{z}$ on a pixel-by-pixel basis, using the weighted linear least squares regression given by equation 3 (Ebmeier et al., 2012):

$$\mathbf{z} = [\mathbf{G^T W_\phi}^{-1}\, \mathbf{G}]^{-1}\mathbf{G^T W_\phi}^{-1}\mathbf{d}. \quad (3)$$

where $\mathbf{W}_\phi$ is a square weighting matrix with diagonal elements of σ_{max}^2, the maximum variance in each interferogram, and off-diagonal elements set to 0 (which ignores any covariance in atmospheric noise between interferograms). The formal variance in $\mathbf{z}$ (σ_z^2) is then $[\mathbf{G^T W_\phi}^{-1}\, \mathbf{G}]^{-1}$, giving an uncertainty (σ_z) of $\sqrt{\left[\mathbf{G^T W_\phi^{-1} G}\right]^{-1}}$. While performing the inversion, incoherent pixels are excluded. The formal error in the topographic change for each pixel is inversely related to the number of interferograms used in the inversion. The uncertainty in the topographic change measurement is therefore greater for pixels that are incoherent in several interferograms.

250 **4.2. ALOS PALSAR**

251 ALOS PALSAR observations of Montserrat cover Phase 5 of extrusive activity at SHV
252 (8 Oct 2009 – 11 Feb 2010). We used scenes acquired in ascending geometry, with the satellite
253 looking approximately east at an incidence angle of 37.6°. From nine ALOS scenes (track 118,
254 frame 320), we constructed eight coherent interferograms — one during the period of quiescence
255 before Phase 5 (13 Aug. – 28 Sept 2009) and seven from after Phase 5 ended (six 46-day
256 interferograms and one 92-day interferogram from 13 Feb. 2010 – 16 Feb. 2011).

257 Interferograms were constructed with the Repeat Orbit Processing software (ROI_PAC)
258 (Rosen et al., 2004) developed at Caltech/JPL, and separate topographic corrections were
259 performed using both the pre-eruptive and 2005 DEMs to give two interferograms for each
260 interval. Interferograms were filtered using a power spectrum filter (Goldstein and Werner,
261 1998) and unwrapped using the branch-cut algorithm of Goldstein et al., 1988. To exploit the
262 maximum range resolution of the PALSAR instrument, interferograms were processed at one
263 look in the range direction and five looks in azimuth direction. The geocoded products have a
264 pixel spacing of 10 m, which is the horizontal resolution of the reference DEMs. We referenced
265 all our interferograms to a pixel north of Centre Hills, as we assume the north of the island
266 remains stable (Fig. 1).

267 Interferograms are considered to be coherent if > 50 % of terrestrial pixels have a
268 coherence > 0.15. This threshold coherence is the mean coherence value over the ocean and
269 should be a representative coherence value of random phase data.

270 We conducted three separate inversions of ALOS interferograms using equation 3 (Table
271 3). We used linear interpolation between estimates of the perpendicular baseline made at the start
272 and end of each interferogram to estimate the baseline at SHV. We used a constant value for v

273 (37.6°) and *r* (854852 m), as these values vary by less than 1 % over the island of Montserrat,
274 which is several orders of magnitude less than the uncertainties introduced by our estimated
275 atmospheric noise. We assumed there was no deformation or topographic change over the
276 intervals covered by the interferograms, so each inversion provides an estimate of the
277 topographic change up to the latest SAR acquisition used in that inversion

278 Inversion **A95-11** estimates the topographic change between the pre-eruptive DEM and
279 Feb. 2011 (Fig. 2a), inversion **A05-11** estimates the topographic change between the Nov. 2005
280 DEM and Feb. 2011, and inversion **A05-09** estimates the topographic change from November
281 2005 to the single coherent interferogram formed between acquisitions on 13 August and 28
282 September 2009 (Fig. 3b). Phase 5 of activity at Montserrat began on 8 October 2009, so this
283 interferogram gives an estimate of the topographic change due to Phases 3 and 4 (Wadge et al.,
284 2014a). Taking the difference between inversion **A95-11** and inversion **A05-11** gives the
285 topographic change between pre-1995 and Nov. 2005 (Fig. 3a), while the difference between
286 inversion **A05-11** and inversion **A05-09** gives the change between Sep. 2009 and Feb. 2011 (Fig.
287 3c; Table 3). We estimated the bulk net volume of new material for each inversion by integrating
288 the topographic change values over areas affected by volcanic activity (Fig. 2c) and multiplying
289 by the area of a pixel (100 m^2).

290 We estimated the amplitude of the noise in each interferogram, which is assumed to be
291 predominantly due to variations in tropospheric water vapour, by calculating the variance of
292 pixel phase values. Pixels within 3 km of the lava dome were masked for the variance estimation,
293 to avoid including topographic change signal in the noise estimate. The standard deviation
294 estimates are in the range 1.1–1.7 cm, which is typical for a tropical volcano with an elevation of
295 ~1 km (Ebmeier et al., 2013a; Parker et al., 2015). These noise estimates form the σ_{max}^2 term in

296 equation 3 and therefore translate into formal error estimates in the topographic change
297 inversions (Section 4.4).

298 **4.3. TanDEM-X processing**

299 TanDEM-X interferograms were constructed from Coregistered Single look Slant range
300 Complex (CoSSC; the basic TDX data format provided by DLR) images using the
301 Interferometric SAR Processor of the GAMMA software package (Werner et al., 2000). The
302 TDX image was treated as the master and the image from TSX is set to be the slave for
303 interferometric processing. Perpendicular baselines calculated from orbit data were halved, to
304 account for the difference in path length for the bistatic case compared to repeat pass InSAR
305 (equation 2) (Krieger et al., 2007; Kubanek et al., 2015a). Interferograms were processed using
306 four looks in the range and azimuth directions. The images were filtered using an adaptive
307 density filter (Goldstein et al., 1998) and unwrapped using a minimum cost flow method (Werner
308 et al., 2002). Geocoding was performed using the Nov. 2005 DEM, giving a final grid spacing of
309 10 m.

310 Unwrapping errors were manually corrected and the phase converted to elevation using
311 equation 2. This inversion **T05-13** estimates the topographic change between the Nov. 2005
312 DEM and the TDX acquisition on 19 Nov. 2013. A residual linear phase ramp remained, so a
313 best fitting plane was found and removed from each image (Poland, 2014). The TanDEM-X
314 interferogram observes layover and shadow effects caused by the steep sides of the dome (locally
315 steeper than 40°, Stinton et al., 2014). Slopes with a component of dip, in the satellite line of
316 sight, steeper than the incidence angle of the satellite (31.3°), are incoherent. Coherence in the
317 TDX interferograms is very high (> 0.9) apart from areas affected by shadow or layover. The

DEM produced from inversion **T05-13** (equivalent to the topographic change shown in Fig. 2c added to the pre-eruption DEM – Fig. 1a) is provided in the supplementary material.

4.4. Uncertainties

4.4.1. Formal estimation

The formal uncertainties for each inversion vary from pixel to pixel, depending on the number of interferograms that are coherent at each pixel and the variance of those interferograms. Pixels that have seven coherent interferograms in inversions **A95-11** and **A05-11** have errors of ~20 m. Where five or fewer interferograms are coherent, the errors rise to 27 m or greater.

The areas with the greatest uncertainties are steeply dipping slopes, especially on the west side of the lava dome, Gage's and Chance's peaks, where slopes facing the east-looking ascending satellite view suffer from incoherence due to layover. Centre Hills and South Soufrière Hills are covered in dense vegetation, which remains incoherent even in 46-day ALOS PALSAR interferograms, giving larger errors or gaps in data. At distal deposits, the error is often greater than the deposit thickness (< 20 m). Integrating the formal errors for height change to make estimates of the volume change therefore often leads to uncertainties in the volume estimate that are greater than the estimate itself.

4.4.2. Empirical estimation

The change in topography from the pre-eruptive DEM to the 2005 DEM is limited to the lava dome and proximal valleys filled with volcanic products (Wadge et al., 2006a; Jones, 2006). There should therefore not be any change in topography north of Centre Hills between inversion **A95-11** and inversion **A05-11** (Table 3). We can use the magnitude of the difference in topographic change between the two inversions in this area to make an empirical estimate of the

magnitude of the errors. Using an arbitrarily sized box containing 40000 pixels, we calculate the mean and standard deviation of pixel topographic change values (Fig. 2a).

Inversion **A95-11** has a mean topographic change of 3.1 m and a standard deviation of 10.1 m. Inversion **A05-11** has a mean of 2.7 m and a standard deviation of 8.7 m (Table 3). The difference between the two has a mean topographic change of 0.4 m and a standard deviation of 4.3 m (Fig. 2d). These standard deviation values are a factor of two better than the formal errors from the inversion, suggesting that we may be able to recover topographic changes of a lower amplitude than the formal error. Indeed, in the distal sections of some valleys, infilling is still visible even though the magnitude is less than our formal uncertainties.

The topographic change estimated by inversion **T05-13** (Table 3), in the 40000 pixel box north of Centre Hills has a mean of −2.8 m and a standard deviation of 9.3 m. The errors in elevation measured by a single TDX interferogram are therefore approximately the same as the errors in the ALOS inversion. In comparison, for the single ALOS interferogram used in inversion **A05-09**, the mean change is 3.5 m and the standard deviation is 15.9 m.

A contribution towards the errors in observed topographic change north of Centre Hills comes from uncertainties in the pre-eruptive/2005 DEMs, which are estimated to have a vertical accuracy of about 10 m (Wadge and Isaacs, 1988; Odbert and Grebby, 2014). A possible explanation for the non-zero mean change in our reference area could also be due to InSAR measurements penetrating farther through vegetation than the optical images used to construct the pre-eruptive DEM (Wadge and Isaacs, 1988). The L-band radar of ALOS will penetrate farther through vegetation than the shorter wavelength X-band radar of TDX, however this effect is negligible on the unvegetated recent eruption deposits.

Other TDX estimates of topographic change at volcanoes have found similar elevation difference measurements for vegetated areas not affected by volcanism. Poland, 2014, measured areas of no topographic change at Kilauea, Hawai'i, and in heavily vegetated areas, found mean change of ± 2 m and standard deviation of ~8 m in DEMs calculated from single TDX interferograms. Albino et al., 2015, found a mean of −4.2 m and standard deviation of 5.5 m for dense vegetation at Nyamulagira, D.R.Congo, by measuring the difference between two DEMs constructed from 11 TDX interferograms. Both studies observed smaller standard deviations for measurements of old lava flows; therefore, our uncertainties in the TDX topographic change measurements on areas covered by post-1995 deposits may be lower than those measured in the vegetated area in the north of Montserrat.

5. RESULTS

We use our InSAR-derived topographic change measurements to build up a time series of surface change at Montserrat (Fig. 3). From our inversions (Table 3) we divide the eruption into three time intervals — pre-1995–2005 (Phases 1 and 2), 2005–2009 (Phases 3 and 4) and 2009–2011 (Phase 5). We are able to measure the maximum thickness of new material at each time interval and to integrate over the area covered by deposits to make estimates of the net onshore volume change. Submarine deposits are not imaged by InSAR; therefore, we are unable to estimate the volume contribution from PDCs that carried material offshore. The volume of these deposits can be measured using repeated bathymetric surveys and accounts for approximately 60 % of the total erupted volume at SHV (e.g. Le Friant et al., 2010; Odbert et al., 2015).

5.1. Dome growth and collapse

5.1.1. 1995–2005

386 During Phases 1 and 2, there were numerous cycles of lava dome growth, followed by
387 partial or complete dome removal in collapse events (Wadge et al., 2009, 2014a). In particular,
388 the collapse of 13 July 2003 that ended Phase 2 removed about 200 million cubic metres of dome
389 and talus, mostly into the sea to the east (Herd et al., 2005). The net topographic change of the
390 dome in the 1995–2005 period (Fig. 3a) is dominated by this event. We observe remnants of the
391 pre-collapse dome 50 to 100 m thick preserved in the northern part of the dome, and talus
392 deposits up to 230 m thick preserved in the upper White River valley (Fig. 4a). Up to 150 m of
393 the 400-year-old, pre-eruption Castle Peak dome that occupied English's Crater were also
394 removed in the 2003 collapse (difference between grey polygon and black line in Fig. 4b).

395 ***5.1.2. 2005–2009***

396 We observe the height of the dome increase by up to 250 m between Oct. 2005 and Sept.
397 2009 (Fig. 3b) (difference between black and red lines in Fig. 4e). This growth is presumed to
398 have occurred entirely after the 20 May 2006 collapse, which removed all of the dome that grew
399 between August 2005 and May 2006 and some residual mass from the 2003 dome (Loughlin et
400 al., 2010). The post 20 May dome is mostly symmetrical, with slightly more growth to the west
401 (Fig. 3b). We also observe 100–150 m of talus deposition in the upper Tar River Valley and
402 Gage's Fan (difference between black and red lines in Fig. 4b). We assume that deposits within
403 the old English's Crater walls are part of the lava dome, while deposits outside the old crater
404 walls are talus and pyroclastic material.

405 ***5.1.3. 2009–2011***

406 During Phase 5, parts of the dome grew in height by up to 100 m, while the summit
407 elevation changed little (Table 4), consistent with photogrammetry measurements (Stinton et al.,
408 2014). New growth on the north side of the dome is visible in Fig. 4e, and deposition of an

409 additional 100 m of talus into Gage's fan can be seen in Fig. 4b (difference between red and blue
410 lines). The dome at the end of lava effusion in 2010 is relatively symmetric about an axis running
411 east–west but with preferential growth to the west especially visible in the TDX data (Fig. 3d and
412 4b).

413 The excavation of an amphitheatre by the 11 Feb. 2010 partial dome collapse is visible to
414 the north of the dome (Fig. 3c and 4a). The upper part of the back wall of the crater left by the
415 collapse is visible in Fig. 4b. The collapse amphitheatre is 100 m deep and 450 m wide relative
416 to the pre-Phase 5 surface (Fig. 3c). Stinton et al. (2014) using photogrammetry and theodolite
417 measurements, estimated the crater to be 125 m deep compared to the surface just before the
418 collapse on 11 Feb. 2010, suggesting an additional 25 m of growth on the north side of the dome
419 during Phase 5 before the collapse, although this could also be attributed to uncertainties in the
420 two estimates.

421 ***5.1.4. Pre-eruption–Post-Phase 5***

422 By integrating the topographic change values from the pre-1995 DEM for every pixel
423 within the English's Crater walls, we measure the net bulk volume of the current SHV dome to
424 be 118 ± 46M m^3 with ALOS and 125 ± 18M m^3 with TDX. This net volume figure accounts for
425 material removed from the pre-eruption Castle Peak dome, as well as that added and removed
426 during the eruption. Using an average vesicularity for the dome of 13 % (Sparks et al., 1998), we
427 estimate a dense rock equivalent (DRE) dome volume of 102–108M m^3. This value will
428 underestimate the true volume of the lava dome, as the volume change of incoherent areas is not
429 included, but the effect is probably minor as only 5 % and 7 % of the pixels on the dome in
430 ALOS and TDX inversions, respectively, are incoherent.

431 ***5.1.5. Differences between ALOS and TDX observations***

There is general agreement to within error between TDX and ALOS over the dome (Table 4; difference between blue and green lines in Fig. 4). TDX appears to show slightly more dome growth to the west of English's crater (Fig. 4b) and slight differences in the depth and shape of the base of the 2010 collapse (Fig. 4e). There is also disagreement in the thickness of talus deposits on the steepest part of Gages fan (between 1000–1500 m in Fig. 4b). This is likely due to loss of signal from TDX because west-facing slopes approach the satellite incidence angle (TDX is affected more strongly by steep slopes because it has a 31.3° incidence angle, less than the 37.6° incidence angle of ALOS). The paired patch of incoherence and negative topographic change observed in the centre of the dome by TDX (Fig. 2c) is likely due to a similar effect on a locally steeper section of the dome. There is much better agreement between the two satellites on south and east facing talus slopes.

5.2. Flow deposits and valley fill

Surrounding the lava dome throughout the eruption was an apron of talus with an angle of repose of 37 degrees (Wadge et al., 2008). The talus apron graded downslope into PDC deposits, mainly produced by collapses of material from the dome (Wadge et al., 2009; Wadge et al., 2010). The distribution of flow deposits changed over the course of the eruption, as valley infilling caused PDCs to overflow into neighbouring valleys (Table 5).

5.2.1. 1995–2005

Figure 3a and 4a show that the thickest subaerial deposits during Phases 1–2 were in White River to the south of the dome, with up to 230 m of deposition at the head of the valley, just outside the rim of English's Crater. The cumulative thickness of PDC deposits decreases with distance down the valley to ~60 m where the pre-eruptive valley entered the sea, and where a delta deposit now sits.

There was also near complete infilling of Fort Ghaut to the west (Fig. 4d), by PDCs that continued downstream to destroy the town of Plymouth in 1997 (e.g. Sparks et al., 1998; Sparks et al., 2002; Wadge et al., 2014a). Deposition to the north was concentrated mainly in Mosquito Ghaut, with thinner deposits in Tuitt's and Tyers Ghauts (Fig. 4c, Table 5).

5.2.2. 2005–2009

Most of the observed valley infilling during Phases 3–4 occurs in the Tar River Valley to the east, refilling the erosional scar left by the 13 July 2003 dome collapse (Fig. 3b). Distal deposition is difficult to observe due to long wavelength (2–5 km) atmospheric gradients in the ALOS data, which have a magnitude equivalent to ± 80 m elevation (Fig. 3b, between 0–300 m in Fig. 4d).

5.2.3. 2009–2011

Deposition during Phase 5 was more widely distributed than in previous phases, including the first deposits in Gingoes Ghaut and Farm River and the most distal deposits in the Belham Valley and White's Ghaut (Table 5)(Stinton et al., 2014). There was also up to 140 m of deposition in Spring Ghaut — the first flows from Gages fan to overspill to the south from Fort Ghaut (Fig. 4d). InSAR infill measurements proximal to the dome agree within error to spot thickness values estimated from the width of shadow zones in radar amplitude images (Wadge et al., 2011).

5.2.4. Pre-eruption–Post-Phase 5

The cumulative maximum net height change (Table 5) rarely equals the sum of the maximum changes for the separate time periods, as the location of greatest net infilling within each valley changes over time. The thickest deposits are in Gages Fan to the west of the dome and the White River south of the dome and reach nearly 300 m in places.

478 The total bulk volume of onshore PDC deposits (excluding the dome) is 450 ± 370M m^3
479 measured by ALOS and 390 ± 280M m^3 measured by TDX (Fig. 2). Using a void-free density of
480 2600 kg/m^3 and a bulk density for the PDC deposit of 2000 kg/m^3 (Sparks et al., 1998; Wadge et
481 al., 2010), we calculate DRE volumes for the two datasets of 350 ± 280M m^3 and 300 ± 220M
482 m^3, respectively. As with the lava dome, these volumes are likely to be underestimates due to
483 incoherence, especially in the upper parts of Spring Ghaut, Fort Ghaut, Gingoes Ghaut and
484 White River, where steep west-facing slopes suffer from layover.
485 There will also be an underestimate of the volume and height change of new subaerial
486 deposits, which have built the coast out since 1995. The thickness change and therefore volume
487 of these deposits is calculated relative to sea level, rather than the pre-eruptive bathymetry,
488 therefore the submarine component needed to bring these deposits to sea level is not accounted
489 for. Montserrat has a shallow submarine shelf 20–60 m deep (Le Friant et al., 2004), so the
490 thickness of new subaerial deposits is likely to be underestimated by at least 20 m. Wadge et al.,
491 2010, gave an estimate for the near coast sediment DRE volume of 113M m^3, while Odbert et al.,
492 2015, estimated the volume of the submarine portion of new land to be 25M m^3 DRE.
493 ***5.2.5. Differences between ALOS and TDX observations***
494 There is good agreement in the cumulative change estimated by both ALOS and TDX,
495 (Table 5). Slight variations may be due to uncertainties in the measurements and redistribution of
496 material between 2011 and 2013 through erosion, rockfalls and lahars.
497 For valley deposits on Montserrat, TDX retrieves a much sharper image than ALOS (Fig.
498 2f compared with Fig. 2e). In order to reduce noise caused by temporal decorrelation, the ALOS
499 data are more heavily filtered than TDX. This overfiltering leads to smearing of the signal, so the
500 observed expression of deposits has a lower amplitude and longer wavelength. This effect is

most apparent in White's Ghaut (difference between blue and green lines in Fig. 4c), where the shape of the 2011 surface measured by ALOS is unrealistically similar to the shape of the pre-eruptive/2005 surface, while the 2013 surface measured by TDX shows much more realistic valley infilling by PDC deposits.

TDX is also able to retrieve thinner deposits in the distal parts of valleys, which are missed by ALOS. This is due to the presence of atmospheric noise in the ALOS data caused by temporal variations in the tropospheric water vapour field, which are not present in the TDX bistatic image. Atmospheric artefacts are visible to the west of the island in Fig. 2a, where they obscure thin deposits in Fort Ghaut and the Belham River Valley, observed by TDX in Fig. 2c.

6. DISCUSSION

6.1. Volume budget

InSAR data from ALOS and TanDEM-X have been used to estimate the change in surface topography of Montserrat associated with the eruption of Soufrière Hills Volcano. There is good agreement in the cumulative volume change estimated by both sensors, and results broadly match those of previous studies based on ground and airborne observations (Wadge et al., 2011; Stinton et al., 2014; Odbert et al., 2015). In comparison with the results of Odbert et al., 2015, we observe greater volume in subaerial PDC deposits, but less volume in the dome, although the total DRE volume is almost identical. The inconsistency is likely due to difficulty in distinguishing between PDC deposits, talus slope, and the dome core based on InSAR data alone, or could be a result of the considerable uncertainty that exists in both methods. The lava dome boundary we used is based on the English's Crater wall and therefore does not include talus in

523 White River/Upper Fort Ghaut, which is considered by Stinton et al., 2014, to be part of the
524 dome.

525 The total combined DRE volume of the lava dome and subaerial pyroclastic deposits
526 measured by InSAR is 424 ± 304M m^3 (ALOS) or 401 ± 231M m^3 (TDX). Our measured values
527 of the subaerial deposits are similar to the 406M m^3 estimated by Odbert et al., 2015 based on a
528 combination of the 2010 LiDAR DEM with the dome volume estimates of Stinton et al., 2014.
529 The total DRE volume for the eruption is estimated to be 1063M m^3, from photogrammetry and
530 theodolite surveys, supplemented by ground based LiDAR, radar, field measurements, and
531 bathymetric surveys (Le Friant et al., 2004, 2010; Wadge et al., 2010, 2014a; Stinton et al.,
532 2014). The subaerial deposits, which have remained on Montserrat since the start of the eruption,
533 therefore account for 38–40 % of the total erupted volume. The remaining 60–62 % of erupted
534 material is therefore located in coastal deposits, deep submarine deposits, and distal airborne ash
535 deposits, consistent with measurements from bathymetry (e.g. Le Friant et al., 2010).

536 **6.2. Measuring topographic change**

537 InSAR data presented here have a number of advantages compared to traditional methods
538 for observing topography. In comparison to optical methods, such as photogrammetry and
539 LiDAR, the ability of InSAR to see through clouds and at any time of day, combined with a
540 wider field of view, provides much more comprehensive spatial coverage. Satellite-based sensors
541 are able to capture imagery of the entire island, even during eruptive periods when deploying
542 terrestrial sensors in the south of the island sometimes proved too hazardous. While ground-
543 based methods may provide more frequent measurement of the topography than satellite
544 observations, no individual terrestrial sensor is able to image the entirety of the deposition field,

545 so results from multiple instruments need to be combined to provide complete topographic
546 information.

547 InSAR should be especially useful if activity were to resume. By combining multiple
548 sensors and acquisition geometries it should be possible to make observations of the dome every
549 few days (Table 2). In comparison, optical methods can require days to weeks before the weather
550 is clear enough to make observations. Spaceborne platforms are also not reliant on instruments
551 being installed at a volcano before an eruption begins — background acquisitions made during
552 periods of quiescence can be used to form new interferograms as soon as eruptive behaviour
553 starts or resumes. However, during extrusive activity topographic measurements will be limited
554 to bistatic sensors (e.g., TDX) because the monostatic method requires a stable, post-eruptive
555 surface.

556 While the overall results from ALOS and TanDEM-X are similar, there are several
557 notable small-scale differences. The lower incidence angle of the TDX acquisitions relative to
558 ALOS results in loss of signal at a shallower slope angle in the TDX data. This is apparent to the
559 west of Chance's Peak and South Soufrière Hills (Fig. 2). The southern end of Fig. 4a (green line
560 between 4800 and 5000 m along profile) shows significant errors in the TDX data on a west-
561 facing slope, which are not as significant in the ALOS data. Errors caused by radar shadow and
562 layover (Section 3.2) could be potentially reduced by combining InSAR data from ascending
563 (satellite looking east) and descending (satellite looking west) viewing geometries (Kubanek et
564 al., 2015a).

565 Due to the lack of atmospheric noise in the bistatic TDX data, the surface derived from
566 TDX is smoother in coherent areas (e.g. difference between blue and green lines between 2600
567 and 3200 m along Fig. 4b). Unfiltered ALOS interferograms are not coherent enough to retrieve

568 topographic information over the lava dome and steeper slopes. In order to improve the
569 coherence of the ALOS data, the ALOS interferograms were filtered more heavily than TDX.
570 This over-filtering has lead to smearing of the ALOS data in some places, most clearly visible in
571 Whites Ghaut (difference between blue and green lines in Fig. 4c). Due to this difference in
572 filtering, it is impossible to distinguish post-Phase 5 (2011–2013) topographic changes from
573 processing artefacts.

574 Since February 2010, there have been numerous rockfalls and rain generated lahars,
575 which have redistributed material from the lava dome and talus fans downhill. The post-Phase 5
576 lahar deposits are 2–3 m thick in the lower reaches of the Belham Valley (A. Stinton., pers.
577 comm.). This elevation difference is within error of our InSAR measurements on Montserrat, and
578 therefore these deposits would be difficult to distinguish, even between different TanDEM-X
579 acquisitions.

580 There are some notable disadvantages to InSAR measurements compared with other
581 techniques. The steep slopes and dense vegetation of Montserrat mean that spatial coverage of
582 the island is often limited, especially with shorter wavelength C-band and X-band sensors
583 (Wadge et al., 2002, 2006a, 2011). Revisit intervals of individual satellites are still on the order
584 of days to weeks, meaning that it may be impossible to distinguish individual flows which occur
585 on timescales of minutes to hours (Wadge et al., 2011). The largest consideration for repeat-pass
586 InSAR on Montserrat is potentially atmospheric noise. The magnitude of atmospheric noise in
587 single interferograms gives uncertainties of over 40 m in the InSAR-derived topography (Fig. 2b
588 and 2c). This noise leads to errors upwards of 250 % in volume estimates between individual
589 repeat-pass interferograms.

590 Atmospheric effects can be reduced through stacking or using weather models; however,
591 both techniques are computationally expensive and reduce the effectiveness of InSAR as a rapid
592 operational technique. In addition, commonly used large-scale weather models such as the
593 European Centre for Medium-range Weather Forecasts (ECMWF) ERA-Interim and North
594 American Regional Reanalysis (NARR) only account for the stratified component of
595 tropospheric water vapour, and do not model the higher amplitude, shorter wavelength turbulent
596 component (e.g. Elliott et al., 2008; Lofgren et al., 2010; Pinel et al., 2011; Parker et al., 2015).
597 Modelled atmospheric phase delays using NARR for inversion **A05-09** only account for 6 m of
598 measured topographic change. In order to model and correct for turbulent water vapour a higher
599 resolution weather model such as the Weather Research and Forecasting Model (WRF), or
600 corrections from GPS may be needed (e.g. Wadge et al., 2006a; Gonget al., 2010; Nico et al.,
601 2011).
602 The ability to image the complete deposition field at an erupting volcano, irrespective of
603 weather conditions, still provides a great improvement on many ground-based monitoring
604 techniques. TanDEM-X bistatic mode provides the facility to potentially map topographic
605 changes at high resolution every 11 days, which could provide vital information about the
606 evolution of hazard at active volcanoes. The techniques outlined here could be applied to any
607 volcano extruding lava, even those with thin basaltic flows (e.g. Poland, 2014; Albino et al.,
608 2015, Kubanek et al., 2015b) and would be particularly useful at ongoing, long-lived eruptions
609 and in settings where terrestrial monitoring is limited. At Montserrat, should a sixth phase of lava
610 extrusion begin, satellite radar observations could image changes to the lava dome and
611 pyroclastic deposits on a daily to weekly basis, rather than the broad overview provided here.
612

7. CONCLUSIONS

We have used L-band monostatic (2010–2011) and X-band bistatic (2013) InSAR to estimate the change in topography due to the eruption of Soufrière Hills Volcano between 1995 and 2010. We observe maximum elevation changes of 290 ± 10 m on the lava dome and 250 ± 10 m in valleys proximal to the dome. We measure the total mean DRE volume of subaerial deposits from the eruption since 1995 to be 400 ± 230M m^3. Large uncertainties are introduced into the measurements due to loss of coherence in areas of layover and shadow, and also temporal decorrelation in repeat-pass InSAR.

We show that bistatic InSAR image pairs collected by TanDEM-X have an absolute vertical accuracy of less than 10 m, similar to inverting multiple repeat-pass interferograms from ALOS. Both the bistatic and monostatic InSAR methods provide a more complete quantification of deposits on Montserrat than any single ground-based technique. Knowledge of topographic change during an eruption is important for updating hazard models to take into account evolving volcano morphology, as well as improving geophysical models and other analyses. The ability of InSAR to provide timely estimates of topographic changes over time could therefore provide a valuable dataset for understanding the state of eruption, as well as hazard assessment at erupting volcanoes.

ACKOWLEDGEMENTS

We thank R.S.J. Sparks, I.M. Watson, M.E. Pritchard and the staff of the Montserrat Volcano Observatory, especially A. Stinton and K. Pascal for useful discussions and comments. We thank D. Dzurisin and two anonymous reviewers, whose comments greatly improved this manuscript. ALOS data were provided by Japan Aerospace Exploration Agency (JAXA) via the Alaska

636 Satellite Facility (ASF). TanDEM-X data were provided by Deutsches Zentrum für Luft- und
637 Raumfahrt e. V. (DLR; German Space Agency) through proposal NTI_INSA0237. DA is
638 supported by a NERC studentship. JB, SE and GW are supported by NERC-COMET. JB and SE
639 are supported by STREVA. This work forms part of the CEOS Volcano Pilot for Disaster Risk
640 Reduction.
641

642 **REFERENCES**

643 Albino, F., B. Smets, N. D'Oreye, and F. Kervyn, 2015, High-resolution TanDEM-X DEM: An
644 accurate method to estimate lava flow volumes at Nyamulagira Volcano (D. R. Congo): Journal
645 of Geophysical Research: Solid Earth, v. 120(6), p. 4189–4207, doi:10.1002/2015JB011988.
646

647 Anderson, K., and P. Segall, 2011, Physics-based models of ground deformation and extrusion
648 rate at effusively erupting volcanoes: Journal of Geophysical. Research: Solid Earth, v. 116(7),
649 B07204, doi:10.1029/2010JB007939.
650

651 Biggs J., S.K. Ebmeier, W.P. Aspinall, Z. Lu, M.E. Pritchard, R.S.J. Sparks, and T.A. Mather,
652 2014, Global link between deformation and volcanic eruption quantified by satellite imagery:
653 Nature communications, v. 5, doi:10.1038/ncomms4471
654

655 Blong, R., 1984, Volcanic hazards. A sourcebook on the effects of eruptions: Academic Press,
656 425 p.
657

658 Bürgmann, R., P. A. Rosen, and E. J. Fielding, 2000, Synthetic Aperture Radar Interferometry to
659 Measure Earth's Surface Topography and Its Deformation, Annual Review of Earth and
660 Planetary Sciences, v. 28(1), p. 169–209, doi:10.1146/annurev.earth.28.1.169.
661
662 Carrivick, J. L., V. Manville, and S. J. Cronin, 2008, A fluid dynamics approach to modelling the
663 18th March 2007 lahar at Mt. Ruapehu, New Zealand: Bulletin of Volcanology, v. 71(2), p. 153–
664 169, doi:10.1007/s00445-008-0213-2.
665
666 Cashman, K. V., and R. S. J. Sparks, 2013, How volcanoes work: A 25 year perspective:
667 Geological Society of America Bulletin, v. 125(5-6), p. 664–690, doi:10.1130/B30720.1.
668
669 Chaussard, E., F. Amelung, and Y. Aoki: 2013, Characterization of open and closed volcanic
670 systems in Indonesia and Mexico using InSAR time series: Journal of Geophysical Research:
671 Solid Earth, v. 118(8), p. 3957–3969, doi:10.1002/jgrb.50288.
672
673 Cole, P., V. Bass, T. Christopher, and C. Eligon, 2010, Report to the Scientific Advisory
674 Committee on volcanic activity at Soufrière Hills Volcano, Montserrat: report on activity
675 between 28 February 2010 and 31 October 2010: Montserrat Volcano Observatory Open File
676 Report, OFR 10–02.
677
678 Cole, P. D., E. S. Calder, T. H. Druitt, R. Hoblitt, R. Robertson, R. S. J. Sparks, and S. R. Young,
679 1998, Pyroclastic flows generated by gravitational instability of the 1996-97 Lava Dome of

680 Soufrière Hills Volcano, Montserrat: Geophysical Research Letters, v. 25(18), p. 3425–3428,
681 doi:10.1029/98GL01510.
682
683 Cole, P. D., P. J. Smith, A. J. Stinton, H. M. Odbert, M. L. Bernstein, J. C. Komorowski, and
684 R. Stewart, 2014, Chapter 5 Vulcanian explosions at Soufrière Hills Volcano, Montserrat
685 between 2008 and 2010: Geological Society, London, Memoirs, v. 39(1), p. 93–111,
686 doi:10.1144/M39.5.
687
688 Dietterich, H. R., M. P. Poland, D. A. Schmidt, K. V. Cashman, D. R. Sherrod, and A. T.
689 Espinosa, 2012, Tracking lava flow emplacement on the east rift zone of Kīlauea, Hawai‘i, with
690 synthetic aperture radar coherence: Geochemistry, Geophysics, Geosystems, v. 13(5),
691 doi:10.1029/2011GC004016.
692
693 Druitt, T. H., 1998, Pyroclastic density currents: Geological Society, London, Special
694 Publications, v. 145(1), p. 145–182, doi:10.1144/GSL.SP.1996.145.01.08.
695
696 Druitt, T. H., S. R. Young, B. Baptie, C. Bonadonna, E. S. Calder, A. B. Clarke, P. D. Cole, C. L.
697 Harford, R. A. Herd, R. Luckett, G. Ryan, and B. Voight, 2002, Episodes of cyclic Vulcanian
698 explosive activity with fountain collapse at Soufrière Hills Volcano, Montserrat: Geological
699 Society, London, Memoirs, v. 21(1), p. 281–306, doi:10.1144/GSL.MEM.2002.021.01.13.
700
701 Dvorak, J. J., and D. Dzurisin, 1993, Variations in magma supply rate at Kilauea Volcano,
702 Hawaii: Journal of Geophysical Research, v. 98(B12), p. 22,255, doi:10.1029/93JB02765.

Ebmeier, S., J. Biggs, T. Mather, J. Elliott, G. Wadge, and F. Amelung, 2012, Measuring large topographic change with InSAR: Lava thicknesses, extrusion rate and subsidence rate at Santiaguito volcano, Guatemala: Earth and Planetary Science Letters, v. 335-336, p. 216–225, doi:10.1016/j.epsl.2012.04.027.

Ebmeier, S. K., J. Biggs, T. A. Mather, and F. Amelung, 2013a, Applicability of InSAR to tropical volcanoes: insights from Central America: Geological Society, London, Special Publications, v. 380(1), p. 15–37, doi:10.1144/SP380.2.

Ebmeier, S. K., J. Biggs, T. A. Mather, and F. Amelung, 2013b, On the lack of InSAR observations of magmatic deformation at Central American volcanoes: Journal of Geophysical Research: Solid Earth, v. 118(5), p. 2571–2585, doi:10.1002/jgrb.50195.

Elliott, J. R., J. Biggs, B. Parsons, and T. J. Wright, 2008, InSAR slip rate determination on the Altyn Tagh Fault, northern Tibet, in the presence of topographically correlated atmospheric delays, Geophysical Research Letters, v. 35(12), doi:10.1029/2008GL033659.

Farr, T. G., P. A. Rosen, E. Caro, R. Crippen, R. Duren, S. Hensley, M. Kobrick, M. Paller, E. Rodriguez, L. Roth, D. Seal, S. Shaffer, J. Shimada, J. Umland, M. Werner, M. Oskin, D. Burbank, and D. Alsdorf, 2007, The Shuttle Radar Topography Mission: Reviews of Geophysics, v. 45(2), RG2004, doi:10.1029/2005RG000183.

726 Fink, J. H., and R. W. Griffiths, 1998, Morphology, eruption rates, and rheology of lava domes:
727 Insights from laboratory models: Journal of Geophysical Research, v. 103(B1), p. 527,
728 doi:10.1029/97JB02838.
729
730 Fournier, T. J., M. E. Pritchard, and S. N. Riddick, 2010, Duration, magnitude, and frequency of
731 subaerial volcano deformation events: New results from Latin America using InSAR and a
732 global synthesis: Geochemistry, Geophysics, Geosystems, v. 11(1), doi:10.1029/2009GC002558.
733
734 Goldstein, R. M., and C. L. Werner, 1998, Radar interferogram filtering for geophysical
735 applications: Geophysical Research Letters, v. 25(21), p. 4035–4038, i:10.1029/1998GL900033.
736
737 Goldstein, R. M., H. A. Zebker, and C. L. Werner, 1988, Satellite radar interferometry: Two-
738 dimensional phase unwrapping: Radio Science, v. 23(4), p. 713–720,
739 doi:10.1029/RS023i004p00713.
740
741 Gong, W., F. Meyer, P. Webley, D. Morton, and S. Liu, 2010, Performance analysis of
742 atmospheric correction in InSAR data based on the Weather Research and Forecasting Model
743 (WRF): in 2010 IEEE International Geoscience and Remote Sensing Symposium, pp. 2900–
744 2903, IEEE, doi:10.1109/IGARSS.2010.5652267.
745
746 Gregg, T. K. P., and J. H. Fink, 1996, Quantification of extraterrestrial lava flow effusion rates
747 through laboratory simulations: Journal of Geophysical Research, v. 101(E7), 16,891,
748 doi:10.1029/96JE01254.

749

750 Guest, J. E., and J. B. Murray, 1979, An analysis of hazard from Mount Etna volcano: Journal of
751 the Geological Society, v. 136(3), p. 347–354, doi:10.1144/gsjgs.136.3.0347.
752
753 Guzzetti, F., S. Peruccacci, M. Rossi, and C. P. Stark, 2007, Rainfall thresholds for the initiation
754 of landslides in central and southern Europe: Meteorology and Atmospheric Physics, v. 98(3-4),
755 p. 239–267, doi:10.1007/s00703-007-0262-7.
756
757 Hanssen, R. F., 2001, Radar Interferometry: Data Interpretation and Error Analysis: Springer
758 Science & Business Media, 308 pp.
759
760 Harris, A. J., W. I. Rose, and L. P. Flynn, 2003, Temporal trends in lava dome extrusion at
761 Santiaguito 1922–2000: Bulletin of Volcanology, v. 65(2-3), p. 77–89, doi:10.1007/s00445-002-
762 0243-0.
763
764 Harris, A. J. L., J. Dehn, and S. Calvari, 2007, Lava effusion rate definition and measurement: a
765 review: Bulletin of Volcanology, v. 70(1), p. 1–22, doi:10.1007/s00445-007-0120-y.
766
767 Herd, R. A., M. Edmonds, and V. A. Bass, 2005, Catastrophic lava dome failure at Soufrière
768 Hills Volcano, Montserrat, 12–13 July 2003: Journal of Volcanology and Geothermal Research,
769 v. 148(3-4), p. 234–252, doi:10.1016/j.jvolgeores.2005.05.003.
770

771 Hubbard, B. E., M. F. Sheridan, G. Carrasco-Núñez, R. Díaz-Castellón, and S. R. Rodríguez,
772 2007, Comparative lahar hazard mapping at Volcan Citlaltépetl, Mexico using SRTM, ASTER
773 and DTED-1 digital topographic data: Journal of Volcanology and Geothermal Research,
774 v. 160(1-2), p. 99–124, doi:10.1016/j.jvolgeores.2006.09.005.
775
776 Huggel, C., D. Schneider, P. J. Miranda, H. Delgado Granados, and A. Kääb, 2008, Evaluation
777 of ASTER and SRTM DEM data for lahar modeling: A case study on lahars from Popocatépetl
778 Volcano, Mexico: Journal of Volcanology and Geothermal Research, v. 170(1-2), p. 99–110,
779 doi:10.1016/j.jvolgeores.2007.09.005.
780
781 Hutchison, W., N. Varley, D. M. Pyle, T. A. Mather, and J. A. Stevenson, 2013, Airborne
782 thermal remote sensing of the Volcan de Colima (Mexico) lava dome from 2007 to 2010:
783 Geological Society, London, Special Publications, v. 380(1), p. 203–228, doi:10.1144/SP380.8.
784
785 Jones, L., 2006, Monitoring landslides in hazardous terrain using terrestrial LiDAR: an example
786 from Montserrat: Quarterly Journal of Engineering Geology and Hydrogeology, v. 39(4), p. 371–
787 373, doi:10.1144/1470-9236/06-009.
788
789 Kauahikaua, J., K. V. Cashman, T. N. Mattox, C. C. Heliker, K. A. Hon, M. T. Mangan, and C.
790 R. Thornber, 1998, Observations on basaltic lava streams in tubes from Kilauea Volcano, island
791 of Hawai'i, Journal of Geophysical Research, v. 103(B11), p. 27303–27323,
792 doi:10.1029/97JB03576.
793

794 Krieger, G., A. Moreira, H. Fiedler, I. Hajnsek, M. Werner, M. Younis, and M. Zink, 2007,
795 TanDEM-X: A Satellite Formation for High-Resolution SAR Interferometry: IEEE Transactions
796 on Geoscience and Remote Sensing, v. 45(11), p. 3317–3341, doi:10.1109/TGRS.2007.900693.
797
798 Kubanek, J., M. Westerhaus, A. Schenk, N. Aisyah, K. S. Brotopuspito, and B. Heck, 2015,
799 Volumetric change quantification of the 2010 Merapi eruption using TanDEM-X InSAR:
800 Remote Sensing of Environment, v. 164, p. 16–25, doi:10.1016/j.rse.2015.02.027.
801
802 Kubanek, J., J. A. Richardson, S. J. Charbonnier, & L.J. Connor, 2015, Lava flow mapping and
803 volume calculations for the 2012–2013 Tolbachik, Kamchatka, fissure eruption using bistatic
804 TanDEM-X InSAR: Bulletin of Volcanology, v. 77(12), p. 1-13, doi:10.1007/s00445-015-0989-9
805
806 Le Friant, A., C. Harford, C. Deplus, G. Boudon, R. Sparks, R. Herd, and J. Komorowski, 2004,
807 Geomorphological evolution of Montserrat (West Indies): importance of flank collapse and
808 erosional processes: Journal of the Geological Society, v. 161(1), p. 147–160, doi:10.1144/0016-
809 764903-017.
810
811 Le Friant, A., C. Deplus, G. Boudon, N. Feuillet, J. Trofimovs, J.-C. Komorowski, R. S. J.
812 Sparks, P. Talling, S. Loughlin, M. Palmer, and G. Ryan, 2010, Eruption of Soufrière Hills
813 (1995–2009) from an offshore perspective: Insights from repeated swath bathymetry surveys:
814 Geophysical Research Letters, v. 37(19), doi:10.1029/2010GL043580.
815

816 Lipman, P. W., and N. G. Banks, 1987, AA flow dynamics, Mauna Loa 1984: US Geological
817 Survey Professional Paper, v. 1350, p. 1527-1567. http://pubs.usgs.gov/pp/1987/1350/
818
819 Loughlin, S. C., R. Luckett, G. Ryan, T. Christopher, V. Hards, S. De Angelis, L. Jones, and
820 M. Strutt, 2010, An overview of lava dome evolution, dome collapse and cyclicity at Soufrière
821 Hills Volcano, Montserrat, 2005-2007: Geophysical Research Letters, v. 37(19),
822 doi:10.1029/2010GL042547.
823
824 Lu, Z., E. Fielding, M. Patrick, and C. Trautwein, 2003, Estimating lava volume by precision
825 combination of multiple baseline spaceborne and airborne interferometric synthetic aperture
826 radar: the 1997 eruption of Okmok volcano, Alaska: IEEE Transactions on Geoscience and
827 Remote Sensing, v. 41(6), p. 1428–1436, doi:10.1109/TGRS.2003.811553.
828
829 Massonnet, D., and K. L. Feigl, 1998, Radar interferometry and its application to changes in the
830 Earth's surface: Reviews of Geophysics, v. 36(4), 441, doi:10.1029/97RG03139.
831
832 Montgomery, D. R., 2001, Slope distributions, threshold hillslopes, and steady-state topography:
833 American Journal of Science, v. 301(4-5), p. 432–454, doi:10.2475/ajs.301.4-5.432.
834
835 Nico, G., R. Tome, J. Catalao, and P. M. A. Miranda, 2011, On the use of the WRF Model to
836 mitigate tropospheric phase delay effects in SAR interferograms: IEEE Transactions on
837 Geoscience and Remote Sensing, v. 49(12), p. 4970–4976, doi:10.1109/TGRS.2011.2157511.
838

839 Odbert, H., B. Taisne, and J. Gottsmann, 2015, Deposit loading and its effect on co-eruptive
840 volcano deformation: Earth and Planetary Science Letters, v. 413, p. 186–196,
841 doi:10.1016/j.epsl.2015.01.005.
842
843 Odbert, H. M., and S. Grebby, 2014, A note on geographical systems and maps of Montserrat:
844 Geological Society, London, Memoirs, v. 39(1), p. 489–494, doi:10.1144/M39.27.
845
846 Odbert, H. M., G. A. Ryan, G. S. Mattioli, S. Hautmann, J. Gottsmann, N. Fournier, and R. A.
847 Herd, 2014, Volcano geodesy at the Soufrière Hills Volcano, Montserrat: a review: Geological
848 Society, London, Memoirs, v. 39(1), p. 195–217, doi:10.1144/M39.11.
849
850 Ogburn, S. E., E. S. Calder, P. D. Cole, and A. J. Stinton, 2014, The effect of topography on ash-
851 cloud surge generation and propagation: Geological Society, London, Memoirs, v. 39(1), p. 179–
852 194, doi:10.1144/M39.10.
853
854 Parker, A. L., J. Biggs, R. J. Walters, S. K. Ebmeier, T. J. Wright, N. A. Teanby, and Z. Lu,
855 2015, Systematic assessment of atmospheric uncertainties for InSAR data at volcanic arcs using
856 large-scale atmospheric models: Application to the Cascade volcanoes, United States: Remote
857 Sensing of Environment, v. 170, p. 102–114, doi:10.1016/j.rse.2015.09.003.
858
859 Parks, M., J. Biggs, T. Mather, D. Pyle, F. Amelung, M. Monsalve, and L. N. Medina, 2011, Co-
860 eruptive subsidence at Galeras identified during an InSAR survey of Colombian volcanoes
861 (2006–2009): Journal of Volcanology and Geothermal Research, v. 202(3-4), p. 228–240,

862 doi:10.1016/j.jvolgeores.2011.02.007.
863
864 Pinel, V., A. Hooper, S. De la Cruz-Reyna, G. Reyes-Davila, M. Doin, and P. Bascou, 2011,
865 The challenging retrieval of the displacement field from InSAR data for andesitic
866 stratovolcanoes: Case study of Popocatepetl and Colima Volcano, Mexico: Journal of
867 Volcanology and Geothermal Research, v. 200(1-2), p. 49–61,
868 doi:10.1016/j.jvolgeores.2010.12.002.
869
870 Pinel, V., M. Poland, and A. Hooper, 2014, Volcanology: Lessons learned from Synthetic
871 Aperture Radar imagery: Journal of Volcanology and Geothermal Research, v. 289, p. 81–113,
872 doi:10.1016/j.jvolgeores.2014.10.010.
873
874 Poland, M. P., 2014, Time-averaged discharge rate of subaerial lava at Kīlauea Volcano, Hawai'i,
875 measured from TanDEM-X interferometry: Implications for magma supply and storage during
876 2011-2013: Journal of Geophysical Research: Solid Earth, v. 119(7), p. 5464–5481,
877 doi:10.1002/2014JB011132.
878
879 Rosen, P. A., S. Hensley, G. Peltzer, and M. Simons, 2004, Updated repeat orbit interferometry
880 package released: Eos, Transactions American Geophysical Union, v. 85(5), p. 47,
881 doi:10.1029/2004EO050004.
882
883 Ryan, G. A., S. C. Loughlin, M. R. James, L. D. Jones, E. S. Calder, T. Christopher, M. H. Strutt,
884 and G. Wadge, 2010, Growth of the lava dome and extrusion rates at Soufrière Hills Volcano,

885 Montserrat, West Indies: 2005-2008: Geophysical Research Letters, v. 37(19),
886 doi:10.1029/2009GL041477.
887
888 Salzer J. T., M. Nikkhoo, T. R. Walter, H. Sudhaus, G. Reyes-Dávila, M. Bretón and R.
889 Arámbula, 2014, Satellite radar data reveal short-term pre-explosive displacements and a
890 complex conduit system at Volcán de Colima, Mexico: Frontiers in Earth Science, v. 2(12),
891 doi:10.3389/feart.2014.00012
892
893 Sparks, R. S. J., and S. R. Young, 2002, The eruption of Soufrière Hills Volcano, Montserrat
894 (1995-1999): overview of scientific results: Geological Society, London, Memoirs, v. 21(1),
895 p. 45–69, doi:10.1144/GSL.MEM.2002.021.01.03.
896
897 Sparks, R. S. J., S. R. Young, J. Barclay, E. S. Calder, P. Cole, B. Darroux, M. A. Davies, T. H.
898 Druitt, C. Harford, R. Herd, M. James, A. M. Lejeune, S. Loughlin, G. Norton, G. Skerrit, M. V.
899 Stasiuk, N. S. Stevens, J. Toothill, G. Wadge, and R. Watts, 1998, Magma production and
900 growth of the lava dome of the Soufrière Hills Volcano, Montserrat, West Indies: November
901 1995 to December 1997: Geophysical Research Letters, v. 25(18), p. 3421–3424,
902 doi:10.1029/98GL00639.
903
904 Sparks, R. S. J., J. Biggs, and J. W. Neuberg, 2012, Monitoring volcanoes: Science, v.
905 335(6074), p.1310-1311, doi:10.1126/science.1219485
906

907 Stevens, N., V. Manville, and D. Heron, 2003, The sensitivity of a volcanic flow model to digital
908 elevation model accuracy: experiments with digitised map contours and interferometric SAR at
909 Ruapehu and Taranaki volcanoes, New Zealand: Journal of Volcanology and Geothermal
910 Research, v. 119(1-4), p. 89–105, doi:10.1016/S0377-0273(02)00307-4.
911
912 Stinton, A. J., P. D. Cole, H. M. Odbert, T. Christopher, G. Avard, and M. Bernstein, 2014,
913 Dome growth and valley fill during Phase 5 (8 October 2009–11 February 2010) at the Soufrière
914 Hills Volcano, Montserrat: Geological Society, London, Memoirs, v. 39(1), p. 113–131,
915 doi:10.1144/M39.6.
916
917 van Westen, C. J., and A. S. Daag, 2005, Analysing the relation between rainfall characteristics
918 and lahar activity at Mount Pinatubo, Philippines: Earth Surface Processes and Landforms, v.
919 30(13), p. 1663–1674, doi:10.1002/esp.1225.
920
921 Wadge, G., and M. C. Isaacs, 1988, Mapping the volcanic hazards from Soufrière Hills Volcano,
922 Montserrat, West Indies using an image processor: Journal of the Geological Society, v. 145(4),
923 p. 541–551, doi:10.1144/gsjgs.145.4.0541.
924
925 Wadge, G., 2000, A DEM of the volcanic deposits of Soufrière Hills Volcano during 1999:
926 Montserrat Volcano Observatory Open File Report, OFR 00–07.
927

928 Wadge, G., B. Scheuchl, and N. F. Stevens, 2002, Spaceborne radar measurements of the
929 eruption of Soufrière Hills Volcano, Montserrat: Geological Society, London, Memoirs, v. 21(1),
930 p. 583–594, doi:10.1144/GSL.MEM.2002.021.01.27.
931
932 Wadge, G., D. Macfarlane, D. Robertson, A. Hale, H. Pinkerton, R. Burrell, G. Norton, and
933 M. James, 2005, AVTIS: A novel millimetre-wave ground based instrument for volcano remote
934 sensing: Journal of Volcanology and Geothermal Research, v. 146(4), p. 307–318,
935 doi:10.1016/j.jvolgeores.2005.03.003.
936
937 Wadge, G., G. Mattioli, and R. Herd, 2006a, Ground deformation at Soufrière Hills Volcano,
938 Montserrat during 1998–2000 measured by radar interferometry and GPS: Journal of
939 Volcanology and Geothermal Research, v. 152(1-2), p. 157–173,
940 doi:10.1016/j.jvolgeores.2005.11.007.
941
942 Wadge, G., H. Odbert, D. Macfarlane, and M. James, 2006b, The November 2005 DEM of the
943 Soufrière Hills Crater: Montserrat Volcano Observatory Open File Report, OFR 06–02.
944
945 Wadge, G., D. G. Macfarlane, H. M. Odbert, M. R. James, J. K. Hole, G. Ryan, V. Bass, S. De
946 Angelis, H. Pinkerton, D. A. Robertson, and S. C. Loughlin, 2008, Lava dome growth and mass
947 wasting measured by a time series of ground-based radar and seismicity observations: Journal of
948 Geophysical Research, v. 113(B8), B08,210, doi:10.1029/2007JB005466.
949

950 Wadge, G., H. Odbert, and D. Macfarlane, 2009, An AVTIS-based DEM of Soufrière Hills for
951 October 2008: Technical Report, Informal Report to Montserrat Volcano Observatory.
952
953 Wadge, G., R. Herd, G. Ryan, E. S. Calder, and J.-C. Komorowski, 2010, Lava production at
954 Soufrière Hills Volcano, Montserrat: 1995-2009: Geophysical Research Letters, v. 37(19),
955 doi:10.1029/2009GL041466.
956
957 Wadge, G., P. Cole, A. Stinton, J.-C. Komorowski, R. Stewart, A. Toombs, and Y. Legendre,
958 2011, Rapid topographic change measured by high-resolution satellite radar at Soufrière Hills
959 Volcano, Montserrat, 2008–2010: Journal of Volcanology and Geothermal Research, v. 199(1-
960 2), p. 142–152, doi:10.1016/j.jvolgeores.2010.10.011.
961
962 Wadge, G., B. Voight, R. S. J. Sparks, P. D. Cole, S. C. Loughlin, and R. E. A. Robertson,
963 2014a, An overview of the eruption of Soufrière Hills Volcano, Montserrat from 2000 to 2010:
964 Geological Society, London, Memoirs, v. 39(1), p. 1–40, doi:10.1144/M39.1.
965
966 Wadge, G., D. G. Macfarlane, H. M. Odbert, A. Stinton, D. A. Robertson, M. R. James, and
967 H. Pinkerton, 2014b, AVTIS observations of lava dome growth at Soufrière Hills Volcano,
968 Montserrat: 2004 to 2011: Geological Society, London, Memoirs, v. 39(1), p. 229–240,
969 doi:10.1144/M39.13.
970

971 Walker, G. P. L., 1973, Lengths of lava flows [and discussion]: Philosophical Transactions of the
972 Royal Society A: Mathematical, Physical and Engineering Sciences, v. 274(1238), p. 107–118,
973 doi:10.1098/rsta.1973.0030.
974
975 Wang, T., M. Liao, and D. Perissin, 2010, InSAR Coherence-Decomposition Analysis: IEEE
976 Geoscience and Remote Sensing Letters, v. 7(1), p. 156–160, doi:10.1109/LGRS.2009.2029126.
977
978 Watts, R. B., R. A. Herd, R. S. J. Sparks, and S. R. Young, 2002, Growth patterns and
979 emplacement of the andesitic lava dome at Soufrière Hills Volcano, Montserrat: Geological
980 Society, London, Memoirs, v. 21(1), p. 115–152, doi:10.1144/GSL.MEM.2002.021.01.06.
981
982 Werner, C., U. Wegmüller, T. Strozzi, and A. Wiesmann, 2000, Gamma SAR and
983 interferometric processing software: Proceedings of the ERS-Envisat Symposium, Gothenburg,
984 Sweden, 16–20 October 2000.
985
986 Werner, C., U. Wegmüller, T. Strozzi, and A. Wiesmann, 2002, Processing strategies for phase
987 unwrapping for INSAR applications: Proceedings of the European Conference on Synthetic
988 Aperture Radar EUSAR 2002, Cologne, Germany, 4–6 June 2002.
989
990 Wright, R., S. Blake, A. J. L. Harris, D. A. Rothery, 2001, A simple explanation for the space-
991 based calculation of lava eruption rates: Earth and Planetary Science Letters, v. 192, p. 223–233,
992 doi:10.1016/S0012-821X(01)00443-5
993

994 Xu, W., and S. Jónsson, 2014, The 2007–8 volcanic eruption on Jebel at Tair island (Red Sea)
995 observed by satellite radar and optical images: Bulletin of Volcanology, v. 76(2), p. 795,
996 doi:10.1007/s00445-014-0795-9.
997
998 **FIGURE CAPTIONS**
999
1000 **FIG. 1. a)** Hillshaded digital elevation model of the pre-eruptive topography of Montserrat.
1001 Major drainage pathways are shown in yellow: Belham River Valley (BRV), Tyers Ghaut (TyG),
1002 Mosquito Ghaut (MG), Paradise Ghaut (PG), Tuitt's Ghaut (TuG), White's Ghaut (WG), Tar
1003 River Valley (TRV), Fort Ghaut (FG), Spring Ghaut (SG), Gingoes Ghaut (GG), White River
1004 (WR). Key topographic features are labelled: Garibaldi Hill (GH), St. George's Hill (SGH),
1005 Chances Peak (CP), Gage's Mountain (GM). Yellow dot shows location of reference pixel used
1006 in InSAR processing. **b)** Regional map of the northern Lesser Antilles. Blue rectangle shows the
1007 area covered by ALOS ascending track 118, frame 320. Red rectangle shows the area covered by
1008 TanDEM-X ascending track 104. Yellow star shows the location of Soufrière Hills Volcano. **c)**
1009 Timeline of summit elevation changes during the eruption (modified from Wadge et al., 2014a).
1010 Red bars show phases of extrusive activity, white bars are periods of quiescence. Black dashed
1011 lines show partial dome collapse events.
1012
1013 **FIG. 2. a)** Topographic change between 1995 and 2011 from ALOS inversion **A95-11**. The
1014 black dashed line show the mask used for measuring deposit volumes. **b)** Errors associated with
1015 the inversion. **c)** Topographic change between 1995 and 2013 derived from TDX inversion **T05-**
1016 **11**. The black dashed line show the mask used for measuring deposit volumes. **d)** Probability

density function showing measured elevation change for an area of no topographic change (shown by the black boxes labelled reference area in **a** and **c**). **e)** and **f)** Zoomed insets highlighting the differences between ALOS and TDX inversions, respectively. Major drainage pathways are labelled: Tyers Ghaut (TyG), Mosquito Ghaut (MG), Paradise Ghaut (PG), Tuitt's Ghaut (TuG), White's Ghaut (WG).

FIG. 3. Time series of topographic change on Montserrat, showing change in elevation during **a)** Phases 1 and 2, **b)** Phases 3 and 4, **c)** Phase 5, and **d)** cumulative change for the whole eruption. Contours show pre-eruptive topography at 100 m intervals. Dashed grey boxes in **b)** and **c)** show areas affected by atmospheric signal in the 2009 interferogram, which are not included in volume estimates. Dashed black line in **c)** marks the extent of the Feb. 11 2010, partial dome collapse. Major drainage pathways are labelled: Fort Ghaut (FG), Tuitt's Ghaut (TuG), White River (WR), Tar River Valley (TRV), Spring Ghaut (SG), White's Ghaut (WG).

FIG. 4. Profiles through the SHV dome and valleys surrounding the volcano at different times (locations shown on the inset map). Profiles are at a 1:1 scale (no vertical exaggeration) in order to preserve topographic slope. The topographies shown are: pre-eruptive (filled grey polygons), 2005 (solid black lines), 2009 (dashed red lines), 2011 (dot-dashed blue lines) and 2013 (solid green lines). Vertical black dashed lines show the intersection of two orthogonal cross section lines. The uncertainties in each profile are given by the typical errors shown in profile A–A'.

TABLES

1040 **TABLE 1.** Previous digital elevation models derived from ground-based or airborne sensors

Date	Horizontal resolution / m	Source	Additional notes	References
Pre-eruption	25/10	1:25,000 scale map	Digitized map	Wadge and Isaacs, 1988
Feb. 1999	10	Aerial photogrammetry	Modified pre-eruption DEM using ERS coherence mask	Wadge, 2000
Nov 2005	10	Terrestrial LiDAR, AVTIS	Modified pre-eruption DEM	Jones, 2006; Wadge et al., 2006b, 2008;
Sep. 2008	10	AVTIS	Modified pre-eruption DEM	Wadge et al., 2009
Jun. 2010	1	Airborne LiDAR	No coverage > 700 m above sea level	Cole et al., 2010; Odbert et al., 2014

1041

1042 **TABLE 2.** Previous digital elevation models derived from space-based InSAR platforms

Date	Source	Band / λ / cm	Revisit period / days	Horizontal resolution / m	Vertical accuracy / m	References
Jul.1996 – 2000	ERS	C / 5.6	35	25	10	Wadge et al., 2002, 2006a
Sep. 1996	JERS-1	L /	44	No elevation data		Wadge et al.,

– May 1997		23.6				2002
Mar. 1996 – Mar. 1998	Radarsat-1	C / 5.6	24	No elevation data		Wadge et al., 2002
Feb. 2000	Shuttle Radar topography Mission (SRTM)	C / 5.6		30	16	Farr et al., 2007
Oct. 2007 – May 2010	TerraSAR-X	X / 3.1	11	2.5	~5	Wadge et al., 2011
May 2011 – Dec. 2011	COSMO-SkyMed	X / 3.1	16 (1/3/4/8)	10	~5	BGS/EVOSS
Aug. 2009 – Feb. 2011	ALOS	L / 23.6	46	10	~20	This study
Nov. 2013	TanDEM-X	X / 3.1	11	10	9.3	This study

TABLE 3. Inversions of InSAR data

	Reference DEM	Number of interferograms	Date range of interferograms	Interval of topographic change	Mean / m	Std. Dev. / m
A05-11	Pre-eruptive	7	Feb. 2010 – Feb. 2011	2005 – 2011	3.1	10.1
A95-11	Nov. 2005	7	Feb 2010 – Feb. 2011	1995 – 2011	2.7	8.7
A05-09	Nov. 2005	1	Aug. 2009 – Sep. 2009	2005 – 2009	3.5	15.9
T05-13	Nov. 2005	1	Nov. 2013	2005 – 2013	−2.8	9.3

Inversions **A95-11**, **A05-11**, and **A05-09** use ALOS interferograms (Section 4.2), while inversion **T05-13** uses a TanDEM-X interferogram (Section 4.3). For discussion of the mean and standard deviation values, see section 4.4.2.

TABLE 4. Maximum change in elevation of the lava dome by eruptive phase, and dome summit height at the end of Phases 2, 4 and 5.

Phase	Maximum dome growth / m	Dome summit elevation at end of phase / m
1–2	110 ± 30	910 ± 30
3–4	250 ± 40	1010 ± 40
5	100 ± 30	1040 ± 30
Total (ALOS)	260 ± 20	1040 ± 30
Total (TDX)	290 ± 10	1030 ± 10

The total rows are the cumulative topographic change between the pre-eruption DEM and the ALOS and TDX data.

1053

1054 **TABLE 5.** Maximum topographic change for the main valleys radiating outward from SHV.

Valley name	1995–2005 / m	2005–2011 / m	ALOS measured (1995–2011) / m	TDX measured (1995–2013) / m
White River	230 ± 30	70 ± 20	240 ± 20	250 ± 10
Gingoes Ghaut	0 ± 30	50 ± 20	60 ± 20	80 ± 10
Gages Fan/Spring Ghaut	190 ± 30	230 ± 40	290 ± 30	280 ± 10
Tyers Ghaut	60 ± 30	80 ± 20	80 ± 20	80 ± 10
Mosquito Ghaut	70 ± 30	0 ± 20	70 ± 20	80 ± 10
Tuitt's Ghaut	60 ± 30	70 ± 20	100 ± 20	110 ± 10
White's Ghaut	0 ± 30	110 ± 20	110 ± 20	110 ± 10
Tar River Valley	−40 ± 30	70 ± 20	70 ± 20	60 ± 10

1055 We ignore the deposits of Dry Ghaut from Phase 1 (Druitt et al., 2002), and of Farm River (Cole
1056 et al., 2014), which are too thin to measure with InSAR.

Figure 1:

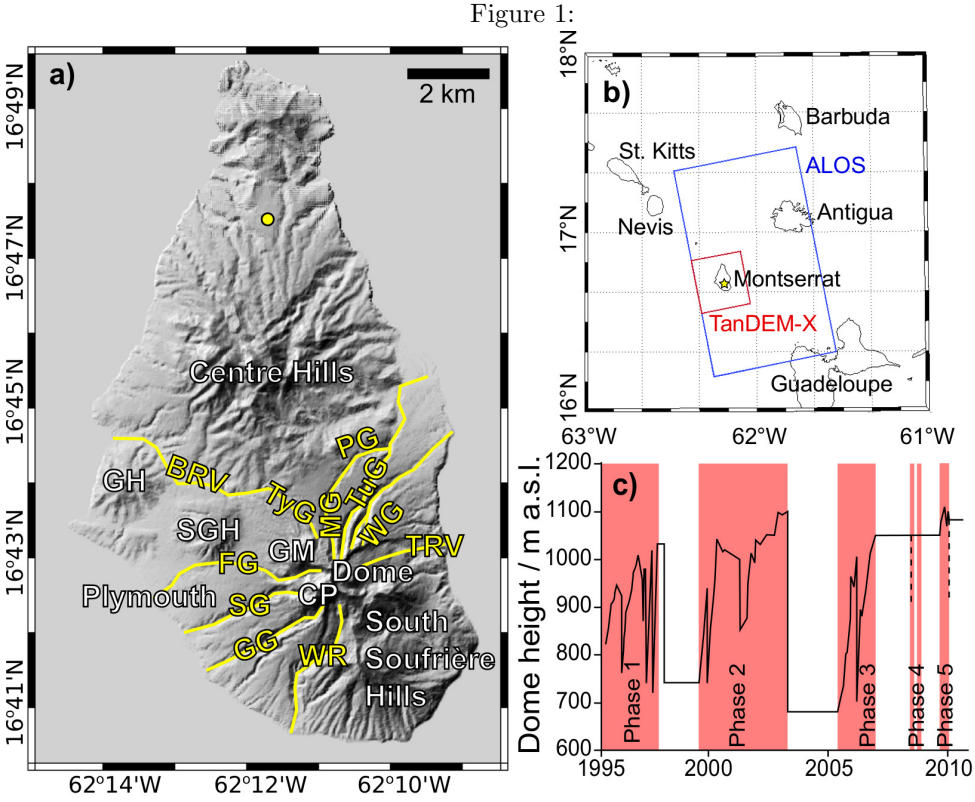

Figure 2:

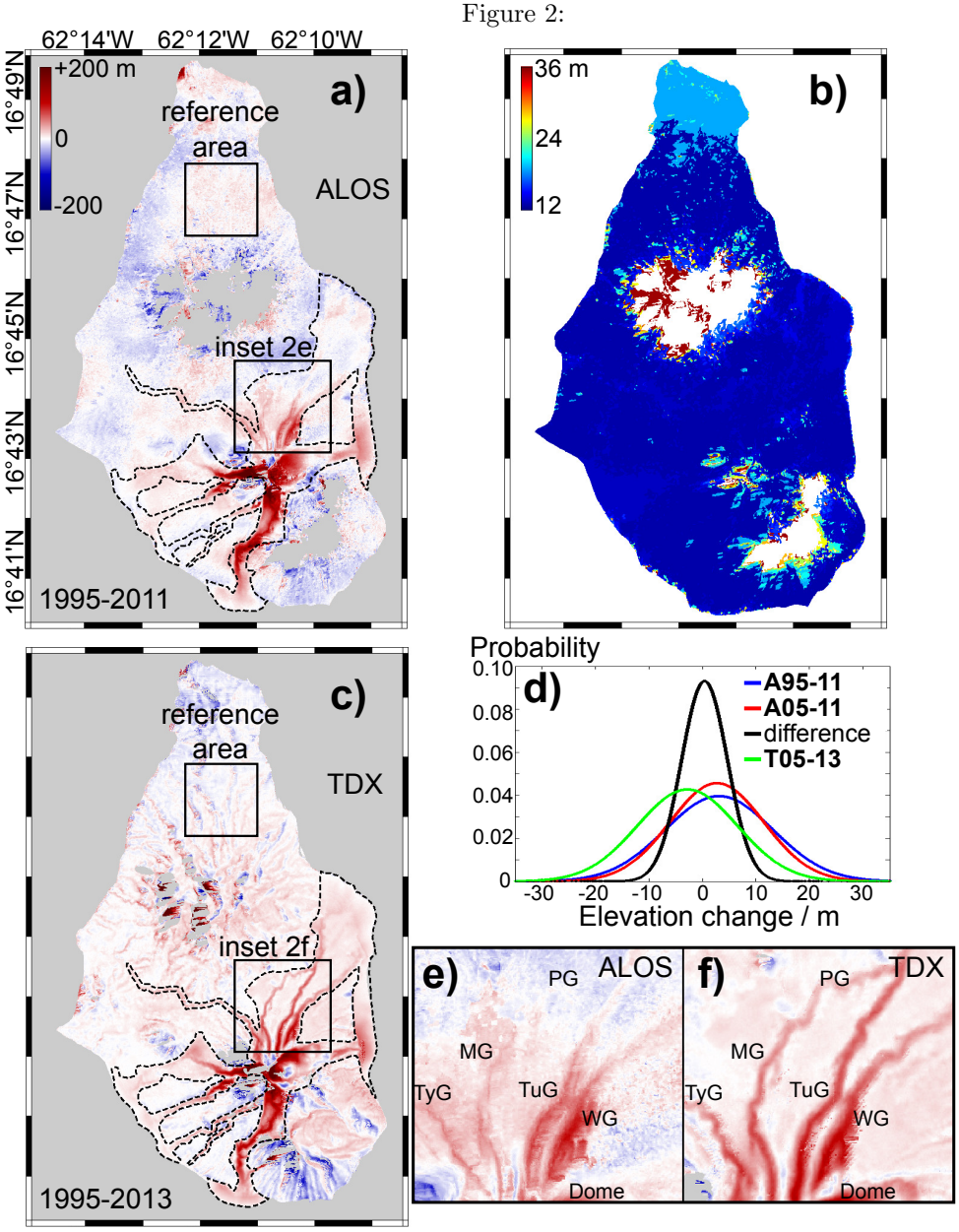
62°14'W
62°12'W
62°10'W
16°49'N
16°47'N
16°45'N
16°43'N
16°41'N
+200 m
0
-200
a)
reference area
ALOS
inset 2e
1995-2011
36 m
24
12
b)
c)
reference area
TDX
inset 2f
1995-2013
Probability
0.10
0.08
0.06
0.04
0.02
0
d)
A95-11
A05-11
difference
T05-13
-30
-20
-10
0
10
20
30
Elevation change / m
e)
ALOS
PG
MG
TyG
TuG
WG
Dome
f)
TDX
PG
MG
TyG
TuG
WG
Dome

Figure 3:

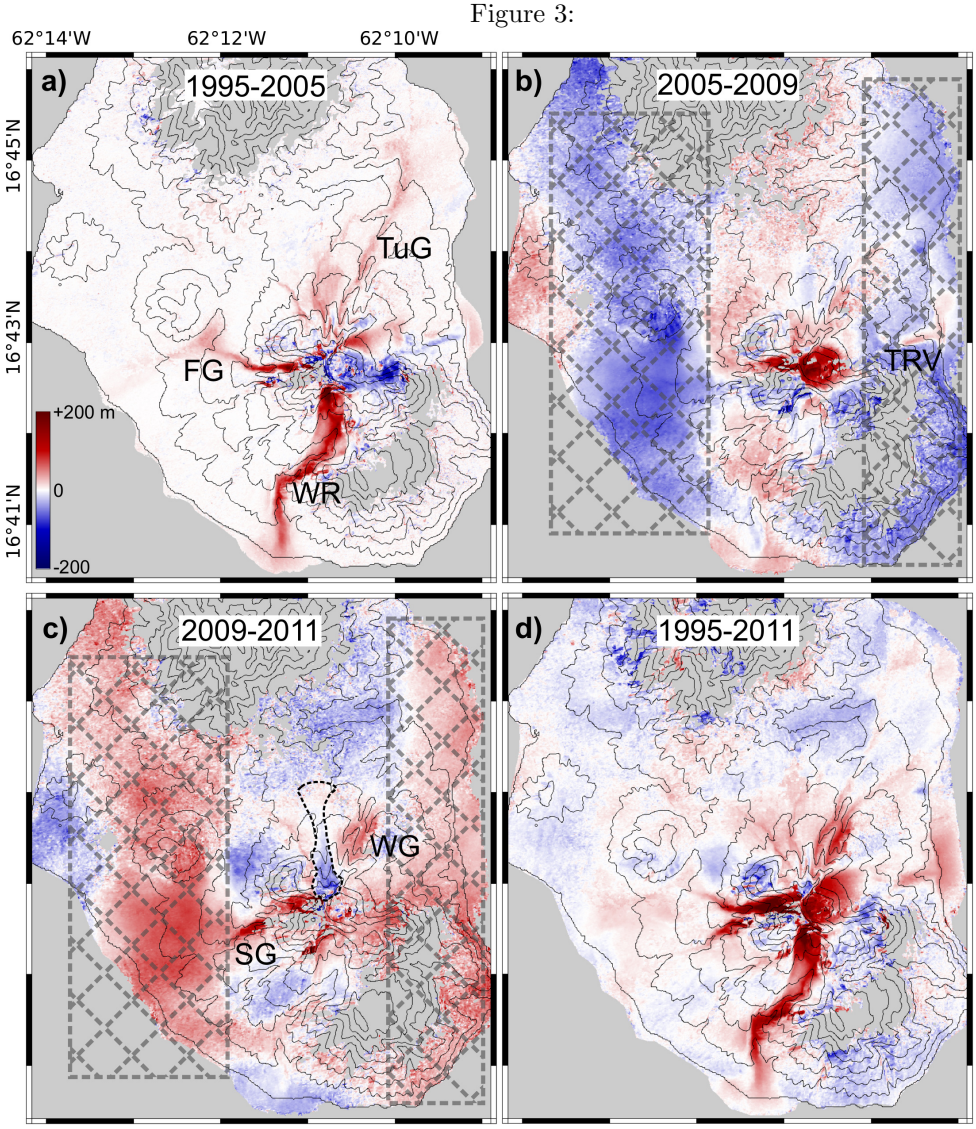
62°14'W
62°12'W
62°10'W
16°45'N
16°43'N
16°41'N
a)
1995-2005
TuG
FG
WR
+200 m
0
-200
b)
2005-2009
TRV
c)
2009-2011
WG
SG
d)
1995-2011

Figure 4:

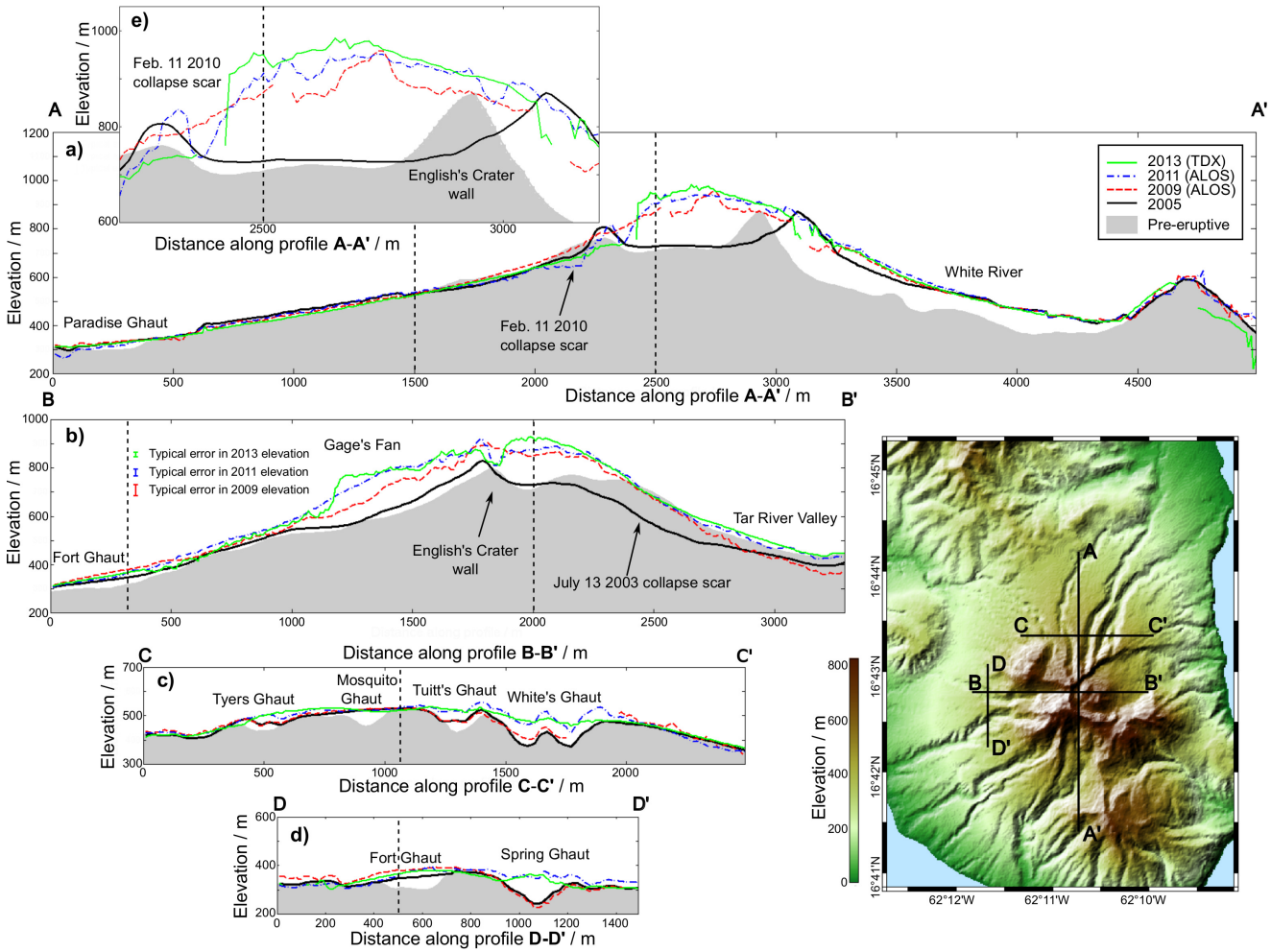
e)
Feb. 11 2010
collapse scar
English's Crater
wall
Elevation / m
Distance along profile A-A' / m
a)
2013 (TDX)
2011 (ALOS)
2009 (ALOS)
2005
Pre-eruptive
White River
Paradise Ghaut
Feb. 11 2010
collapse scar
A
A'
B
B'
b)
Typical error in 2013 elevation
Typical error in 2011 elevation
Typical error in 2009 elevation
Gage's Fan
Tar River Valley
Fort Ghaut
English's Crater
wall
July 13 2003 collapse scar
Distance along profile B-B' / m
C
C'
c)
Tyers Ghaut
Mosquito
Ghaut
Tuitt's Ghaut
White's Ghaut
Distance along profile C-C' / m
D
D'
d)
Fort Ghaut
Spring Ghaut
Distance along profile D-D' / m
16°45'N
16°44'N
16°43'N
16°42'N
16°41'N
62°12'W
62°11'W
62°10'W